Geochemistry Geophysics Geosystems G3

Article
Volume 12, Number 8
11 August 2011
Q08009, doi:10.1029/2011GC003669
ISSN: 1525-2027

Published by AGU and the Geochemical Society

An interdisciplinary investigation of a recent submarine mass transport deposit at the continental margin off Uruguay

Susann Henkel
Alfred Wegener Institute for Polar and Marine Research, Am Handelshafen 12, D-27570 Bremerhaven, Germany

Now at Institute of Geology and Mineralogy, University of Cologne, Zülpicher Str. 49a, D-50674 Cologne, Germany (susann.henkel@uni-koeln.de)

Michael Strasser, Tilmann Schwenk, and Till J. J. Hanebuth
MARUM–Center for Marine Environmental Sciences and Faculty of Geosciences, University of Bremen, Leobener Str., D-28359 Bremen, Germany (mstrasser@marum.de; tschwenk@uni-bremen.de; thanebuth@uni-bremen.de)

Johannes Hüsener
Faculty of Geosciences, University of Bremen, Leobener Str., D-28359 Bremen, Germany (j.huesener@uni-bremen.de)

Gail L. Arnold
Biogeochemistry Department, Max Planck Institute for Marine Microbiology, Celsiusstr. 1, D-28359 Bremen, Germany (glarnold@mpi-bremen.de)

Daniel Winkelmann
Leibniz Institute of Marine Sciences at University of Kiel (IFM-GEOMAR), Wischhofstr. 1-3, D-24148 Kiel, Germany (dwinkelmann@ifm-geomar.de)

Michael Formolo
Department of Geosciences, University of Tulsa, 800 South Tucker Drive, Tulsa, Oklahoma 74104, USA (michael-formolo@utulsa.edu)

Juan Tomasini
Administración Nacional de Combustibles, Alcoholes y Portland, Paysandú s/n esq. Avenida del Libertador, Montevideo, 11100 Uruguay (jtomasini@ancap.com.uy)

Sebastian Krastel
Leibniz Institute of Marine Sciences at University of Kiel (IFM-GEOMAR), Wischhofstr. 1-3, D-24148 Kiel, Germany (skrastel@ifm-geomar.de)

Sabine Kasten
Alfred Wegener Institute for Polar and Marine Research, Am Handelshafen 12, D-27570 Bremerhaven, Germany (sabine.kasten@awi.de)

[1] Assessing frequency and extent of mass movement at continental margins is crucial to evaluate risks for offshore constructions and coastal areas. A multidisciplinary approach including geophysical, sedimentological, geotechnical, and geochemical methods was applied to investigate multistage mass transport deposits (MTDs) off Uruguay, on top of which no surficial hemipelagic drape was detected based on echosounder data. Nonsteady state pore water conditions are evidenced by a distinct gradient change in the sul-

fate (SO_4^{2-}) profile at 2.8 m depth. A sharp sedimentological contact at 2.43 m coincides with an abrupt downward increase in shear strength from ~10 to >20 kPa. This boundary is interpreted as a paleosurface (and top of an older MTD) that has recently been covered by a sediment package during a younger landslide event. This youngest MTD supposedly originated from an upslope position and carried its initial pore water signature downward. The kink in the SO_4^{2-} profile ~35 cm below the sedimentological and geotechnical contact indicates that bioirrigation affected the paleosurface before deposition of the youngest MTD. Based on modeling of the diffusive re-equilibration of SO_4^{2-} the age of the most recent MTD is estimated to be <30 years. The mass movement was possibly related to an earthquake in 1988 (~70 km southwest of the core location). Probabilistic slope stability back analysis of general landslide structures in the study area reveals that slope failure initiation requires additional ground accelerations. Therefore, we consider the earthquake as a reasonable trigger if additional weakening processes (e.g., erosion by previous retrogressive failure events or excess pore pressures) preconditioned the slope for failure. Our study reveals the necessity of multidisciplinary approaches to accurately recognize and date recent slope failures in complex settings such as the investigated area.

Components: 11,900 words, 7 figures, 3 tables.

Keywords: continental margin; pore water geochemistry; slope stability; submarine mass transport.

Index Terms: 0414 Biogeosciences: Biogeochemical cycles, processes, and modeling (0412, 0793, 1615, 4805, 4912); 3002 Marine Geology and Geophysics: Continental shelf and slope processes (4219); 3070 Marine Geology and Geophysics: Submarine landslides.

Received 20 April 2011; **Revised** 28 June 2011; **Accepted** 30 June 2011; **Published** 11 August 2011.

Henkel, S., et al. (2011), An interdisciplinary investigation of a recent submarine mass transport deposit at the continental margin off Uruguay, *Geochem. Geophys. Geosyst.*, *12*, Q08009, doi:10.1029/2011GC003669.

1. Introduction

[2] Increasing numbers of offshore constructions including undersea cables, pipelines, and oil rigs require detailed hazard assessments with regard to submarine mass movement. Reasons for slope failure are multifold and include slope oversteepening, earthquake loading, internal wave activity, rapid sediment accumulation and associated underconsolidation, gas charging, gas-hydrate dissociation, seepage, glacial and hydroisostacy, and volcanic island growth [*Locat and Lee*, 2002]. Gaining reliable data about frequency, causes, and consequences of submarine mass movement in a specific region is often difficult. Hydroacoustic mapping can reveal the presence of slump and slide deposits, but does not allow complete determination of the internal structures of mass transport deposits (MTDs) due to its limited horizontal and vertical resolution. Sedimentological analyses of sediment cores overcome most of these limitations but accurate dating of the slide event, identification of the original trigger mechanism, as well as the identification of relocated coherent sediment blocks still represent major challenges. In the case of very young (tens to hundreds of years old) MTDs, pore water geochemistry can help to recognize the remobilized/transported character of sediment blocks [*de Lange*, 1983; *Zabel and Schulz*, 2001; *Hensen et al.*, 2003]. One of the most important pore water parameters in this regard is the sulfate (SO_4^{2-}) concentration. In marine, "undisturbed" environments the SO_4^{2-} and alkalinity pore water profiles are shaped predominantly by the upward flux of methane (CH_4), SO_4^{2-} concentrations in the bottom water, and sedimentation rates (SRs).

[3] Within the zone of anaerobic oxidation of methane (AOM), microbes use SO_4^{2-} and oxidize CH_4 according to the net equation:

$$CH_4 + SO_4^{2-} \rightarrow HCO_3^- + HS^- + H_2O \quad (1)$$

[e.g., *Barnes and Goldberg*, 1976; *Reeburgh*, 1976; *Boetius et al.*, 2000]. Under steady state conditions, SO_4^{2-} concentrations decrease linearly with depth, while alkalinity increases toward the zone of AOM, where HCO_3^- and HS^- are liberated. In fact, this correlation is a simplification. Linear profiles always show a pore water system being in equilibrium. However, continuous bioirrigation is reflected by nonlinear profiles although the system can be

described as steady state with respect to the depositional conditions.

[4] The depth, at which downward diffusing SO_4^{2-} and upward diffusing CH_4 coexist, is referred to as sulfate-methane transition zone (SMTZ). Drastic changes in SRs, CH_4 fluxes, the intensity of bioirrigation, advective processes, as well as submarine landslides may disrupt the steady state conditions and lead to transient kink shape, concave-up, concave-down, or s-type SO_4^{2-} profiles [e.g., *Aller*, 1983; *Hensen et al.*, 2003; *Kasten et al.*, 2003]. Nonsteady state SO_4^{2-} profiles are therefore sometimes used for geochemical modeling in order to trace back such profound changes in environmental and/or depositional conditions [*Zabel and Schulz*, 2001; *Hensen et al.*, 2003; *Riedinger et al.*, 2005].

[5] Here we present an interdisciplinary approach to examine a supposedly young (i.e., subrecent) MTD at the continental margin off Uruguay. The aim of this study is to overcome the aforementioned problems with respect to the identification and dating of slide deposits by applying a wide range of methods. We exemplarily demonstrate how the link between pore water geochemistry and more conventional submarine landslide investigation methods can be used to detect recent slope failures.

[6] Possible trigger mechanisms for very young submarine landslides can be identified by analyzing the historical record of "extreme" events in the study area that may have been responsible for sediment remobilization. For instance, many studies have shown that the ultimate trigger mechanism for submarine slope failures often relates to earthquakes, even along passive continental margins with very low seismicity [*Hampton et al.*, 1996; *Bryn et al.*, 2005; *ten Brink et al.*, 2009; *Stigall and Dugan*, 2010]. Correlating identified and dated (by means of geochemical analysis) young MTDs with the historical earthquake catalog may thus provide the means of reconstructing recent submarine landslide scenarios as well as assessing the geohazard potential and recurrence of similar events in the future. This approach is applied with respect to the observed young MTD offshore Uruguay.

2. Setting

[7] The continental margin off Uruguay and Argentina was formed during the opening of the South Atlantic in the early Cretaceous [e.g., *Uliana et al.*, 1989; *Hinz et al.*, 1999; *Franke et al.*, 2007]. Extrusive volcanism occurred during the continental breakup and formed thick wedges of igneous rocks underlying the present steep continental slope [*Hinz et al.*, 1999]. The volcanic rocks are covered by a thick succession of generally undisturbed Cretaceous-Tertiary sediments. At present, sedimentation along the margin is strongly influenced by the structure of the water column. Strong contour-parallel currents lead to the formation of depositional and erosional sedimentary features, such as contourite deposits, moats, contouritic channels, and erosional terraces [*Hernández-Molina et al.*, 2009; *Krastel et al.*, 2011]. Most of the research during the past decades focused on oceanographic questions [e.g., *Guilderson et al.*, 2000; *Bianchi et al.*, 2002; *Piola et al.*, 2005; *Möller et al.*, 2008; *Palma et al.*, 2008]. The oceanographic conditions in the upper water column are determined by the highly energetic Brazil-Malvinas Confluence near 38°S [*Brennecke*, 1921; *Deacon*, 1937; *Gordon and Greengrove*, 1986]. In the deeper water column, the northward flowing Antarctic Intermediate Water and the Upper and Lower Circum Polar Deep Water interfinger with the southward flowing North Atlantic Deep Water. A detailed description of the complex water column structure is given by *Piola and Matano* [2001].

[8] Slope failure is a common characteristic at the continental margin off Uruguay and Argentina [*Lonardi and Ewing*, 1971; *Klaus and Ledbetter*, 1988; *Hensen et al.*, 2003; *Krastel et al.*, 2011]. According to *Krastel et al.* [2011], most of the landslides occur in water depths >1,500 m, are comparatively small (with volumes <2 km^3), and are to some extent associated with prominent canyons.

[9] Our study area is located off Uruguay; ~300 km east of the Río de la Plata mouth (Figure 1). *Krastel et al.* [2011] refer to it as the "northern slide area." High amounts of sediment are discharged to the continental margin by the Río de la Plata. Dependent on the wind direction, the suspension freight is mainly transported to the north. However, in particular in the southern summer, the plume may extend to the upper continental slope [*Piola et al.*, 2008] and possibly leads to increased sediment accumulation in the study area. Post rifting Tertiary tectonic activity is generally considered to be insignificant in the study area [*Hinz et al.*, 1999; *Schnabel et al.*, 2008]. However, recent historically documented intraplate seismicity aligned along the Martín García fracture zone or "Salado transfer"

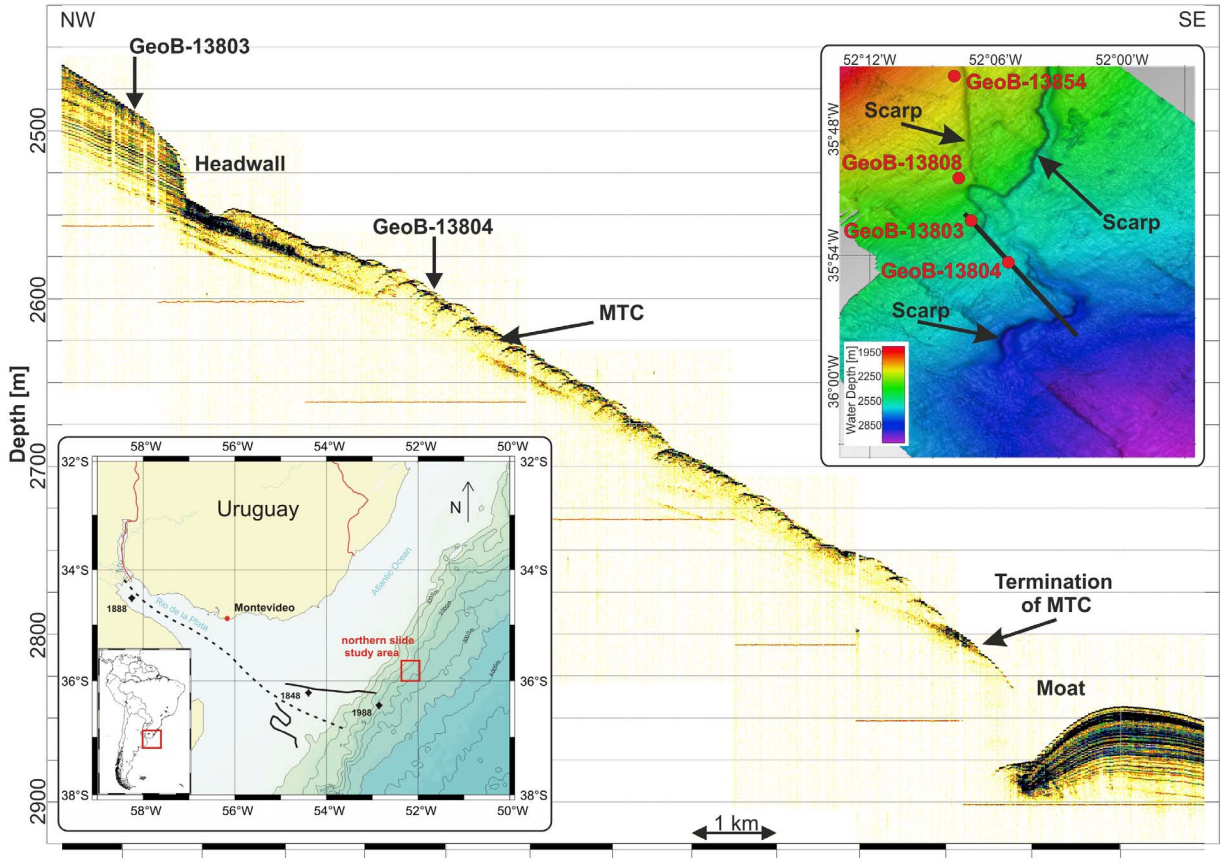

Figure 1. The map on the lower left side shows the location of the study area offshore Uruguay (red frame) and the epicenter of recent earthquakes (black diamonds with dates). The dashed line represents the Salado transfer fault. The multibeam bathymetry of the study area including the location of the Parasound profile, the studied core GeoB 13804 and the core locations GeoB 13803, 13808, and 13854 of which the input parameters for the slope stability analysis were deduced, are shown on the right side. The Parasound profile indicates a mass transport complex (MTC) at the position of core GeoB 13804. The Parasound figure was created using the free software SENT developed by H. Keil, University of Bremen. The depth in meters was calculated using a sound velocity of 1500 m s^{-1}.

(i.e., an inherited extensional tectonic lineament striking NW–SE; Figure 1) suggests present-day tectonic activity in the area, which likely is in a state of active subsidence [*Benavídez Sosa*, 1998]. Earthquakes producing significant macroseismic intensities in the coastal cities of Buenos Aires and Montevideo recently occurred in the years 1848, 1888, and 1988 A.D. [*Benavídez Sosa*, 1998] (Figure 1). The earthquake in 1848 (location of epicenter see Figure 1) could be felt in Montevideo with an intensity of V–VI on the Mercalli Scale [*Benavídez Sosa*, 1998]. The 1888 earthquake occurred close to populated areas in the Río de la Plata estuary between Colonia (Uruguay) and Buenos Aires (Argentina; Figure 1). The epicenter of the 1988 earthquake was located close to our study area and had a body wave magnitude of ~5.2 m_b [*Assumpção*, 1998]. It has not been investigated so far, whether or not such recent seismotectonic activity had influence on sediment dynamics along the continental margin off Uruguay and Argentina. One aim of this study is to test the hypothesis that a recent earthquake was strong enough to initiate retrogressive slope failure in the "northern slide area."

3. Material and Methods

[10] All geophysical data and sample material were gained during cruise M78/3 that took place from 19 May to 6 July 2009. The cruise track, core locations, the bathymetry of the continental slope off Uruguay and Argentina, and general sedimentological characteristics of slope sediments from core data are shown by *Krastel et al.* [2011]. In this study, we focus on site GeoB 13804 (gravity and multiple corer core; for location see Figure 1).

Table 1. Coordinates, Water Depths, and Lengths of All Gravity Cores and Multicorer Cores Investigated in This Study

Core	Device[a]	Latitude	Longitude	Water Depth (m)	Core Length (cm)
GeoB 13803-2	GC	35°52.65′ S	52°07.19′ W	2462	321
GeoB 13804-1	GC	35°54.30′ S	52°05.42′ W	2593	608
GeoB 13804-2	MUC	35°54.26′ S	52°05.43′ W	2593	28
GeoB 13808-1	GC	35°49.85′ S	52°07.76′ W	2300	467
GeoB 13854-1	GC	35°45.54′ S	52°07.89′ W	2109	552

[a]GC, gravity core; MUC, multicorer core.

Additional data from other cores in the study area are used to infer our interpretation and input parameters for stability calculations. The respective data are presented in Figures S1–S4 in the auxiliary material.[1] The following sections briefly summarize the methods used. More details, in particular with respect to bathymetric and sediment echosounder data, are provided by *Krastel et al.* [2011].

3.1. Geophysical Mapping

[11] Sediment echosounder data were collected with the Parasound system (Atlas Hydrographic GmbH), which utilizes the parametric effect to emit a 4 kHz signal in a cone of 4.5–5° opening angle. This configuration results in a vertical resolution of a few decimeters and a horizontal resolution of 7% of the water depths, which is less than 200 m in the study area. Features of smaller dimensions are thus integrated. Details can be found in the work by *Grant and Schreiber* [1990]. Bathymetric data were collected with the Kongsberg EM120 multibeam system. The data were automatically and manually edited to create a grid of 100 m bin size.

3.2. Sampling

[12] The coordinates, water depths, and lengths of all cores investigated in this study are presented in Table 1. The core handling and geochemical sample processing was performed following the standard procedures after *Schulz* [2006]. After recovery, the gravity cores were cut into segments of 1 m length. Syringe samples (3 cm^3) for CH_4 analyses were taken from gravity core GeoB 13804-1 directly during cutting at the lower ends of the segments. The sediment was immediately transferred into 20 ml headspace vials, which were prefilled with 10 ml of a 5 M NaCl solution. The headspace vials were closed, shaken, and stored at 4°C until analysis onshore. Sampling for moisture and density parameters was performed for all of the gravity cores shown in Table 1. Immediately after splitting the segments of the cores into halves, sampling was performed every 50 cm according to Integrated Ocean Drilling Program (IODP) onboard laboratory practices [*Blum*, 1997]. Pore water sampling of gravity core GeoB 13804-1 and the respective mulicorer (MUC) core GeoB 13804-2 was carried out at ~4°C by the use of rhizons [*Seeberg-Elverfeldt et al.*, 2005]. The redox potential (E_H) was measured by use of a punch-in electrode. For the determination of the ^{210}Pb activity, the MUC core GeoB 13804-2 was sliced in 1 to 2 cm intervals. The sediment was transferred into Petri dishes and stored at 4°C until further processing. Sediment samples from the gravity core GeoB 13804-1 were taken using plastic syringes with cut tips. The syringes were sealed and stored frozen at −20°C to avoid alteration of the samples due to microbial activity. A few days after sampling, the syringes were put into impermeable nitrogen-flooded bags, which were kept at −20°C until processing of the samples.

3.3. Geotechnical and Sedimentological Analyses

[13] The undrained shear strength of the sediment was determined onboard using a Wykeham-Farrance cone penetrometer WF 21600 and a Mennerich Geotechnik vane shear device (rotation 90° min^{-1}) following the procedures after *Boyce* [1977] and *Blum* [1997]. Moisture and density parameters were determined according to the IODP shipboard practices [*Blum*, 1997]. Wet and dry mass of the sediment were measured to a precision of 0.01 g using a seagoing weighing device equipped with two electronic balances and a computer-averaging system to compensate for ship motion. Dry volume measurements were performed onshore using helium-displacement pentapycnometers. Sedimentological investigations involved a detailed visual core description and analysis of radiographies.

[1]Auxiliary materials are available in the HTML. doi:10.1029/2011GC003669.

3.4. Pore Water Analyses

[14] Sulfate measurements were performed onboard using a Sykam solvent delivery system coupled to a Waters 430 conductivity detector. Daily standard calibrations using seawater provided by the International Association for the Physical Sciences of the Oceans (IAPSO) were performed. Alkalinity was determined by titration of a 1 ml pore water aliquot with 10–100 mM HCl. For calculating the alkalinity, the equation given by *Schulz* [2006] was used. Sulfide concentrations ($\Sigma H_2S = H_2S + HS^- + S^{2-}$) were analyzed onboard using the methylene blue method of *Cline* [1969]. Phosphate (HPO_4^{2-}) was determined using the photometric method described by *Grasshoff et al.* [1999]. Phosphate samples that contained sulfide were purged with argon prior to the addition of the reagents. Dissolved Fe^{2+} concentrations were determined photometrically at 565 nm after addition of a sample aliquot (1 ml) to 50 μl of Ferrospectral solution to complex the Fe^{2+}. Samples with high concentrations of Fe^{2+} (>1 mg l^{-1}) were pretreated with 10 μl ascorbic acid and diluted with O_2-free artificial seawater prior to complexation. Methane was measured with a Hewlett Packard 5890A gas chromatograph using a splitless injector, a stainless steel Porapak-Q column, and a flame ionization detector. Chromatographic response on the gas chromatograph was calibrated against three different standards with variable concentrations of CH_4. The measured concentrations were corrected for sediment porosity.

3.5. Total Organic Carbon

[15] Total carbon (TC) and inorganic carbon (IC) were determined by measuring dried and homogenized bulk samples using an ELTRA carbon sulfur analyzer at the University of Riverside, California. Total organic carbon (TOC) contents were calculated subtracting IC concentrations from TC.

3.6. Dating of Sediment

[16] Analyses of ^{210}Pb, ^{226}Ra, and ^{137}Cs were performed at the Max Planck Institute for Marine Microbiology in Bremen. The sediment samples were freeze-dried, ground in an agate mortar and subsequently analyzed by nondestructive gamma spectrometry. Sample analyses ran for a minimum of 24 h each. Unsupported ^{210}Pb ($^{210}Pb_{unsupp}$; airborne, not produced in the sediment by decay of ^{226}Ra) was calculated for each depth by subtracting the activity of ^{226}Ra from the activity of ^{210}Pb. Sediment ages were calculated using the C.I.C. (constant initial concentration) and the C.R.S. (constant rate of supply) models of *Robbins* [1978] and *Appleby and Oldfield* [1978].

3.7. Modeling of Sulfate Profile Development

[17] The re-equilibration of the SO_4^{2-} profile at site GeoB 13804 based on molecular diffusion was simulated with the computer software CoTReM, which is a modular, numerical transport and reaction model based on the operator splitting approach. *Adler et al.* [2001] and *Wenzhöfer et al.* [2001] provide detailed descriptions of the software. Similar to our approach, *Hensen et al.* [2003] and *Riedinger et al.* [2005] successfully applied CoTReM to simulate the diffusive re-equilibration of the SO_4^{2-} profile after a submarine landslide and the movement of the SMTZ as a consequence of changing SRs and upward CH_4 fluxes, respectively.

[18] A model length of 8 m was chosen and subdivided into cells of 5 cm thickness. A length of 8 m allows displaying potential changes of the SMTZ depth while inhibiting excessive computing times. The time step to fulfill numerical stability was set to 0.05 years. Analogous to *Hensen et al.* [2003] and *Riedinger et al.* [2005] we used a constant porosity for the simulation. We applied a value of 0.6 that represents the average porosity as measured for the upper 6 m of the sediment column (see Figure S1), the section in which the processes most relevant for our approach (AOM according to equation (1) and downward diffusion of SO_4^{2-}) take place. The transport mechanisms generally considered in the model were molecular diffusion (D_s), bioirrigation, and sediment accumulation. Details can be found in section 5.2. The boundary conditions are given in Table 2 and discussed in section 5.

3.8. Limit Equilibrium Slope Stability Analysis

[19] In order to quantitatively investigate possible trigger scenarios for the observed slope failures we performed a computer-based probabilistic Limit Equilibrium slope stability analysis. This analysis was carried out by using the commercially available software package *Slide* (Rocscience Inc.) that is widely used in geotechnical engineering for slope stability assessments under subaerial conditions, but can be adapted to the subaqueous environment by applying full-saturation and effective stress condition by using the buoyant unit weight in the model scenarios [e.g., *Strasser et al.*, 2007]. The program uses equal-width slices and allows for

Table 2. Parameters and Boundary Conditions for the CoTReM Modeling of the Sulfate Profile at Station GeoB 13804

	Basic Parameters for CoTReM	
Model length (m)	8	
Cell discretisation (cm)	5	
Time step (yr)	0.05	
Porosity φ	0.6	
Temperature (°C)	3.5	
	Boundary Conditions	
	Before Slide	After Slide
Sedimentation rate (cm yr^{-1})	0.08	0.18
Upper Boundary		
SO_4^{2-} (mmol l^{-1})	28	28
CH_4 (mmol l^{-1})	0	0
Lower Boundary		
SO_4^{2-} (mmol l^{-1})	0	0
CH_4 (mmol l^{-1})	40	40
	Diffusion Coefficients[a]	
	D_0	D_{sed}
SO_4^{2-} (cm^2 yr^{-1})	179.5	88.79
CH_4 (cm^2 yr^{-1})	293.6	145.2

[a]Diffusion coefficient in free solution (D_0) calculated for a temperature of 3.5°C and corrected for tortuosity (θ) after *Boudreau* [1997]; $D_{sed} = D_0/\theta^2$, while $\theta^2 = 1 - \ln(\varphi^2)$.

input of a slope profile, subbottom geometry of layers and their geotechnical properties, and a predefined failure surface geometry as reconstructed for prefailure conditions from the Parasound and multibeam bathymetry data and compiled physical property core data gathered during cruise M78/3. Additionally, a pseudostatic acceleration can be used to model the peak ground acceleration generated by earthquakes and to evaluate the seismic slope stability. This parameter implies that the earthquake acceleration is applied over a significantly long period of time so that the induced stresses can be considered constant [*Hampton et al.*, 1996]. Thus, the dynamic response of the sediment is not taken into account. The output factor of safety (FS; i.e., the ratio between the resisting shear strength and the sum of all loading forces (mobilized shear stress)) is calculated using a combined General Limit Equilibrium (GLE)/Morgenstern-Price method [*Morgenstern and Price*, 1965; *Fredlund and Krahn*, 1977].

[20] To account for uncertainties in model input parameters (Table 3), the analyses were performed in a probabilistic mode. Contrary to the deterministic approach that uses one single constant value for each input parameter, the probabilistic approach considers variability and hence uses a mean and standard deviation value. Here, the input data samples are randomly generated using the Monte Carlo sampling method simulating the uncertainty and variability of each input parameter. The FS is calculated for 5000 runs and model outputs reveal the mean FS value of the modeled slope and the corresponding probability of failure (i.e., % of all analyses with FS < 1).

4. Results

[21] Generally, the applied methods refer to data at very different scales. The theoretical vertical resolution of the Parasound data (several decimeters) is reduced by a combination of diffractions, interferences, and side echoes. Pore water data of the gravity core in contrast integrate over a few centimeters, but were gained only in dm scale, whereas visual core description as well as pore water and ^{210}Pb data of the MUC core are accurate to within 1–2 cm. Therefore, different units and decimal places for the vertical scale are used in the following sections depending on the data referred to.

4.1. Geophysical Data

[22] The seafloor in the study area is characterized by a series of three scarps (Figure 1) as described in detail by *Krastel et al.* [2011]. The NW–SE orientated Parasound profile imaging the location of gravity core GeoB 13804 (Figure 1) crosses two of these scarps with heights of 25 m and 50 m (NW

Table 3. Input Parameters for Geotechnical Slope Stability Model[a]

Parameter	Mean Value	Variability	Absolute Minimum	Absolute Maximum
Slope angle (°)	2.25	0.25	2	2.5
Failure depth (mbsf)	75	25	50	100
Unit weight (kN m^{-3})	15.8	1	14.8	16.8
Shear strength at seafloor (kPa)	1	7	0	15
Shear strength gradient with depth (kPa m^{-1})	1.5	0.7	0.4	2.6

[a]General model assumptions: one-layer; infinite slope model; GLE/Morgenstern-Price method; undrained failure; hydrostatic conditions; additional horizontal forces due to horizontal seismic accelerations.

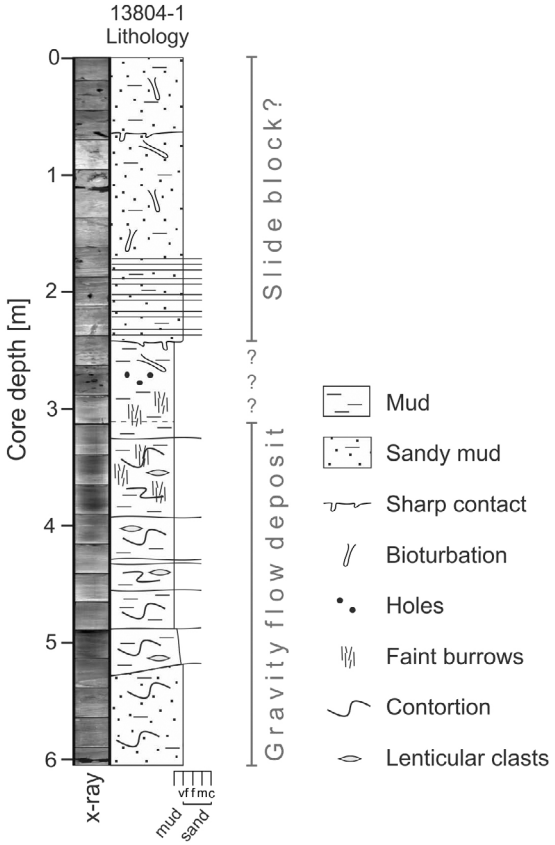

Figure 2. Radiographies and lithological column of gravity core GeoB 13804-1.

and SE, respectively). The deposits in the northwestern part of the profile appear as distinct, parallel layered acoustic facies of moderate amplitude, partly intercalated by thin acoustically transparent layers. The area between both scarps is characterized by an up to 20 m thick and acoustically transparent/chaotic body with hummocky surface located on top of a prolonged reflector. This sediment body pinches out upslope of the southeastern scarp in a water depth of 2800 m. Continuous high-amplitude reflectors showing a convex-upward reflection configuration are imaged downslope of this scarp. Along strike, crosscutting relationships between individual scarps and acoustically transparent/chaotic bodies [*Krastel et al.*, 2011] as well as weakly imaged internal reflection patterns within the body suggest a multistage MTD/mass transport complex (MTC) evolving from reactivation/retrogressive failures along the head scarp. On the Parasound profile shown in Figure 1, the northwestern scarp corresponds to the headwall of the MTC, which here appears as a single landslide body but which was likely formed by several mass wasting events. The section upslope of the headwall shows rather undisturbed sediments. The acoustic parallel layering points to hemipelagic origin, which is confirmed by core data (see Figure S2 for lithological column of gravity core GeoB 13803-2). The convex unit in the southeastern part of the profile (Figure 1) is interpreted as contouritic drift deposit, and the adjacent scarp in 2850 m water depth as a contouritic moat, which redirects and intensifies the ocean currents locally. Similar contouritic features have been observed southwest of our study area [*Krastel et al.*, 2011]. Based on the results of hydroacoustic subsurface imaging methods, no hemipelagic drape overlying the hummocky surface could be identified. Therefore, a relatively young age of the youngest mass transport event is suggested. However, we need to consider that the vertical resolution of the Parasound data is in dm scale (see section 3.1). Therefore, in order to estimate the age of the youngest slide deposit, multidisciplinary analyses on sediment cores needed to be applied, especially to investigate the hypothesized multistage evolution of the MTC.

4.2. Geotechnical and Sedimentological Data

[23] The sedimentological examination of gravity core GeoB 13804-1, which was recovered to investigate the upper part of the MTC (Figure 1), reveals an upper unit (0.00–2.43 m core depth) consisting of soft hemipelagic mud with a succession of several cm thick, undeformed sand layers at 1.80–2.00 m (Figure 2). The sharp boundary of this unit coincides with an abrupt downward increase in shear strength from ~10 kPa to >20 kPa at 2.43 m core depth (Figures 2 and 3). The sediments below this boundary appear to be overconsolidated (as inferred from the high ratio between the undrained shear strength and reconstructed hydrostatic overburden stress [e.g., *Ladd and Foott*, 1974; *Locat and Lee*, 2002] (Figure 3)) and are composed of cohesive mud with sandy layers. Bioturbation has overprinted the contact at 2.43 m and diffused the original structures. The upper part of the core (above 2.79 m) shows macrostructures including filled burrows of up to 1.5 cm in diameter and 12 cm in length. Besides these unambiguous bioturbation structures, several tubelike holes of similar diameter are present at 2.63 m, 2.65 m, and 2.69–2.72 m (Figure 2). Below 2.79 m, macroscopic bioturbation is absent. Only fine bright burrows of 2–15 cm length and approximately 0.5 mm width subvertically penetrate the sediment between 2.79 and 4.37 m. Below 3.07 m, the sediments are fine grained, contain scattered shell fragments and are internally deformed

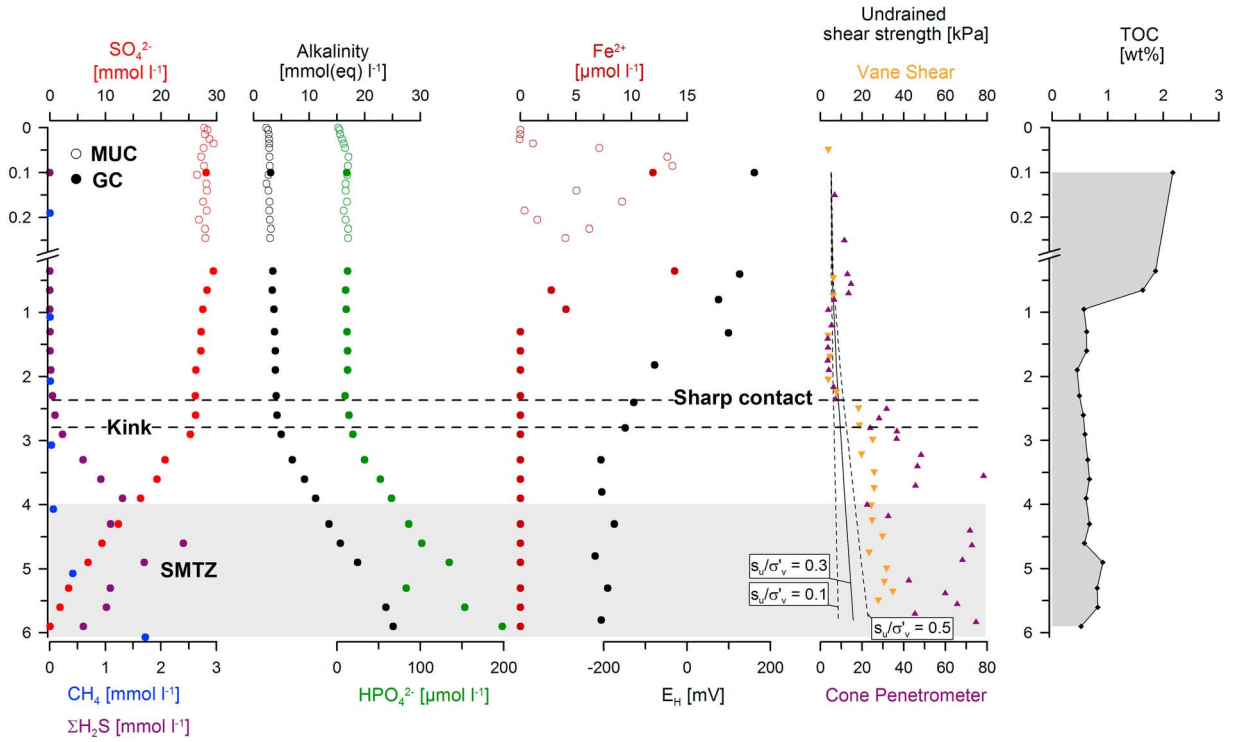

Figure 3. Geochemical pore water and geotechnical data of gravity core GeoB 13804-1 and MUC core GeoB 13804-2. The gray shaded interval represents the SMTZ. Note that the kink in the pore water profiles is located about 0.35 m deeper than the sharp contact. The solid and dashed lines in the undrained shear strength plot indicate Stress History and Normalized Soil Engineering Parameters (SHANSEP [*Ladd and Foott*, 1974]). Ratios for s_u/σ'_v (with s_u = undrained shear strength and σ'_v = vertical effective stress) show trends of under-consolidation, normal consolidation, and overconsolidation (0.1, 0.3, and 0.5, respectively), typical for fine-grained marine sediments [*Locat and Lee*, 2002].

(Figure 2). The radiographs indicate that this lowest section toward the bottom of the core resembles internal flow structures of plastically deformed sediments, as evidenced by distorted mud layers with varying silt content. This unit is interpreted as gravity flow deposit. It correlates to the transparent/chaotic reflection pattern identified in the Parasound data and may also correlate to the MTD described by *Krastel et al.* [2011] in the nearby core GeoB 13807. The overlying succession shows no clear evidence for nonsteady state conditions and allows us to hypothesize that it represents a relocated sediment body that retained its internal structures and that was transported during a recent, smaller slide event.

4.3. Geochemical Data

[24] At site GeoB 13804, the pore water profiles are characteristic for nonsteady state conditions (Figure 3). The SO_4^{2-} concentrations stay more or less constant within the upper 2.8 m and scatter around the typical seawater value of ~28 mM. Below this depth, SO_4^{2-} concentrations strongly decrease. Methane concentrations start to increase at approximately 4.0 m core depth and reach 1.7 mM at the bottom of the core. The SO_4^{2-} and CH_4 profiles overlap producing a broad SMTZ at 4.0–6.0 m core depth, which is characterized by maximum ΣH_2S concentrations of ~2.4 mM at ~4.6 m. Alkalinity and HPO_4^{2-} profiles follow an inverse trend to SO_4^{2-}. The uppermost ~2.8 m of the sediment show low values similar to seawater concentrations; below 2.8 m the concentrations increase with depth. Dissolved Fe^{2+} is present between 0.03 m and 1.0 m with values of up to 14 μM. The E_H values decrease from 161 mV at 0.1 m to −206 mV at 5.8 m core depth.

[25] The TOC concentrations in gravity core GeoB 13804-1 range between 0.4 and 2.2 wt% with the highest values at the core top (Figure 3). Below ~0.9 m core depth, there is not much variation in TOC concentrations (average value ~0.6 wt%).

[26] The activity of $^{210}Pb_{unsupp}$ measured in samples of the MUC core shows an exponential decrease

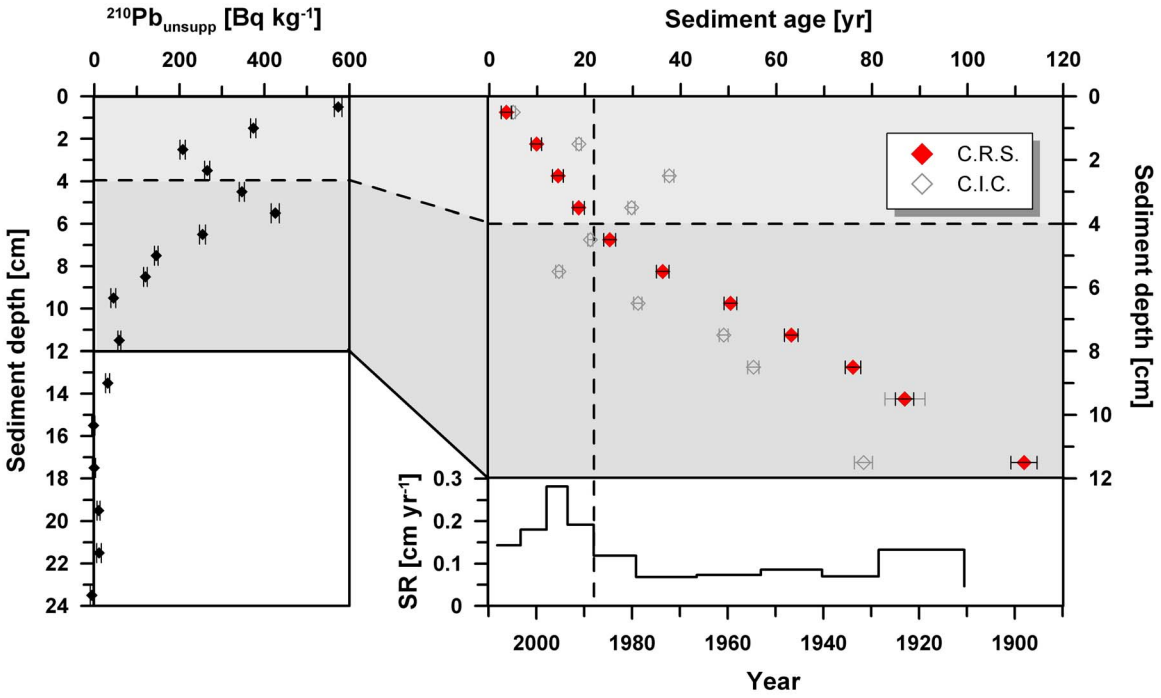

Figure 4. Unsupported ^{210}Pb activity at site GeoB 13804 (MUC core) and sediment ages calculated from $^{210}Pb_{unsupp}$ using the C.I.C. and the C.R.S. model. The sedimentation rates (SRs) appear not to be constant over time. Therefore, the C.R.S. data is valid. A drastic change in SRs happened at about 1988. The average SR from 1888 to 1988 was 0.08 cm yr^{-1}, whereas the average SR from 1988 to 2009 amounted to 0.18 cm yr^{-1}.

with depth but seems to be somehow disturbed between 2 and 4 cm (Figure 4). At 15 cm, $^{210}Pb_{unsupp}$ is completely depleted. We applied the C.I.C. and the C.R.S. models (see 3.6; Figure 4) in order to determine the sediment age and SRs. The C.R.S. data, which are more accurate than the C.I.C. results since they account for SR changes, indicate a sediment age of 112 years at 11.5 cm depth. ^{137}Cs could not be applied as a check for the sediment age, since the activities are extremely low throughout the cored depths. The application of this radioactive element as an age check is generally difficult for regions in the southern hemisphere, where the overall ^{137}Cs inventory is low [e.g., *Tsumune et al.*, 2011]. Around 1988, the SR as determined from the C.R.S. ages increased drastically. The average SR between 1988 and 2009 is 0.18 cm yr^{-1} and thus more than twice as high as the average SR of 0.08 cm yr^{-1} prior to 1988 (Figure 4).

5. Discussion

5.1. Nonsteady State Pore Water Conditions at site GeoB 13804

[27] Generally, the reason for nonsteady state conditions in the pore water system at a particular study site is difficult to assess, because the processes able to cause disequilibrium are numerous. As mentioned above, they include bioirrigation [e.g., *Aller*, 1983; *Aller et al.*, 1996; *Fossing et al.*, 2000], fluid seepage or bubble ebullition of CH_4 [e.g., *Haeckel et al.*, 2007], variations in the diffusive upward flux of CH_4 [e.g., *Kasten et al.*, 2003], and mass transport events [*Zabel and Schulz*, 2001; *Hensen et al.*, 2003]. If some of these processes take place simultaneously, it is practically impossible to reconstruct them based on a single approach.

[28] In the following section, potential scenarios for the development of nonsteady state conditions at site GeoB 13804 are discussed and evaluated in consideration of the complementary data. *Kasten et al.* [2003] and *Riedinger et al.* [2005] demonstrated that sudden variations in the upward CH_4 flux (possibly in combination with extremely high SRs) cause concave rather than kink-shaped profiles. Thus, the observed SO_4^{2-} profile at site GeoB 13804 cannot be explained by such a process. Variability in sulfate reduction rates (SRR) and TOC concentrations play a role in shaping pore water profiles as well. As was shown by *Mazumdar et al.* [2007], high SRs that lead to an enhanced

preservation of TOC may fuel sulfate reduction and result in a steep SO_4^{2-} gradient compared to sites of low SRs and enhanced degradation of TOC by oxygen. However, variations in SRR and TOC with depth might explain concave profiles, but are not suitable to explain kink-shaped profiles as observed at site GeoB 13804. Furthermore, the kink-shaped pore water profiles are not related to a sudden change in TOC concentrations (Figure 3). In the following, we discuss the most probable reasons for the kink-shaped sulfate pore water profile.

5.1.1. Gas Seepage or Fluid Flow

[29] Several tube-like structures in core GeoB 13804-1 at 2.63 m, 2.65 m, and 2.69–2.79 m are suspicious as they appear approximately at the depth of the kink in the sulfate profile (Figures 2 and 3). Possibly, they are a result of ongoing lateral or vertical advection. These structures differ from the unambiguous aforementioned bioturbation structures as they are not filled with sediment. Constant upward release of gas (CH_4 or other hydrocarbons) does not seem to be an explanation for these holes since they appear only above the SMTZ. Upward fluid seepage can result from hydro-fracturing and sudden drainage of marine sediment as a consequence of transient pore pressure increase due to dynamic loading (e.g., earthquake tremor) or due to fast deposition of low-permeable sediments [*Mörz et al.*, 2007]. A vertical advective fluid flow through the entire upper ~2.8 m is, however, unlikely to have caused the observed sulfate profile shape. In fine-grained sediments, upward fluid flow has been shown to produce concave pore water profiles and a condensed redox zonation rather than kink-shaped profiles [*Haese et al.*, 2003]. A lateral fluid flow through the aforementioned open, tubelike structures with a diffusion-dominated transport of chemical species into the surrounding cohesive mud could possibly produce the observed kink-shaped pore water profiles. A lateral flow of SO_4^{2-} rich water, however, would likely be related with more positive values of E_H at the respective depth compared to the underlying sediment. As shown in Figure 3, this is not the case for site GeoB 13804. The value at 2.8 m (−149 mV) shows reducing conditions that follow the overall decrease of redox potential toward the bottom of the core. Therefore we exclude the idea of any advection-controlled process for the formation of the SO_4^{2-} kink at site GeoB 13804.

5.1.2. Mass Transport and Bioirrigation

[30] In general, kink shape SO_4^{2-} profiles can be a consequence of overthrusting of sediment by cohesive slide blocks that carry their initial pore water characteristics downslope [*Zabel and Schulz*, 2001; *Hensen et al.*, 2003]. Given that the SO_4^{2-} gradient in a slide block differs from the gradient in the underlying sediment, the base of the MTD is usually characterized by an inflexion point in the SO_4^{2-} profile. Considerable variation in SO_4^{2-} gradients over small distances as well as SO_4^{2-} concentrations scattering around the concentration in bottom water over the whole lengths of m long gravity cores are known to occur in the study area (e.g., sites GeoB 2803-3 and GeoB 2806-5 [*Bleil et al.*, 1994]) and could reflect local differences in SRs, TOC concentrations, and SRR [*Mazumdar et al.*, 2007]. Thus, the prerequisites for the formation of kink-shaped pore water profiles by mass wasting events at the continental slope off Uruguay are given. The sedimentological data of core GeoB 13804-1 do not give clear evidence for the succession of depositional events (a recent MTD) that affected the study site. However, it also does not exclude that an intact sediment package (possibly in form of a block) was deposited while maintaining its initial pore water signal. The lithological boundary at 2.43 m and the drastic change in shear strength are likely to represent the boundary between the paleosurface and the base of the supposed recently relocated block. Macroscopic bioturbation structures down to 2.79 m depth suggest that this horizon was densely populated by macrofauna. The SO_4^{2-} kink being located approximately at the base of the bioturbation structures can consequently be explained by an exchange of pore water with bottom water down to a paleodepth of ~0.35 m before the most recent mass transport event happened (Figure 5). Additional bioturbation structures above 2.43 m core depth could be "inherited" from an upslope location of initial sediment accumulation. It is unlikely that bioirrigation alone accounts for the formation of the kink in the sulfate profile. Although m deep and cm thick burrows are known to occur in deep-sea sediments [*Löwemark and Schäfer*, 2003], the Fe^{2+} increase at 0.03 m depth at site GeoB 13804 as well as the filling of most of the tubelike structures indicate that right before coring, there was no deep penetration of SO_4^{2-}-rich (and possibly O_2-rich) bottom water through the burrows. Active bioirrigation to such an extent is expected to increase the

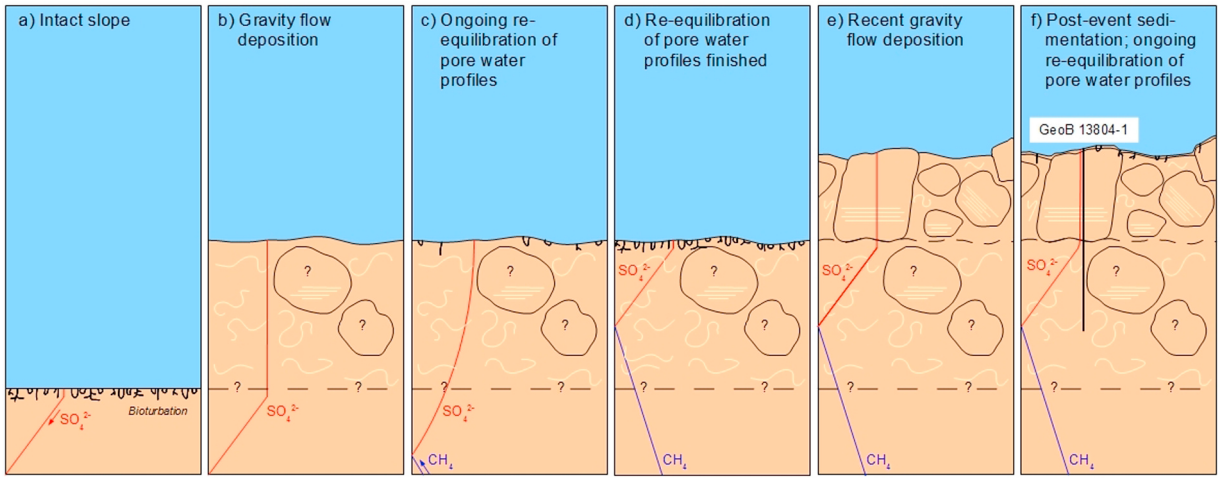

Figure 5. Schematic conceptual model showing the hypothesized depositional scenario for site GeoB 13804. (a–f) The solid lines in show the development of the pore water profiles (red and blue for sulfate and methane, respectively) after the inferred gravity flows as well as bioturbation in phases of low sediment accumulation. The vertical black solid line in Figure 5f represents the position and penetration depth of the gravity corer.

oxygen penetration depth and inhibit the shallow reduction of iron oxides [*Ziebis et al.*, 1996].

[31] We suggest that the kink-shaped pore water profile at site GeoB 13804 is mainly a consequence of a recent MTD (Figure 5). The undisturbed sand layers and the lamination at 1.80–2.00 m core depth, however, indicate primary depositional characteristics likely related to a contouritic depositional environment. This apparent contradiction can be explained by interpreting the sediment package above 2.43 m to result from a mass transport process that did not effectively remold the entire landslide mass, but relocated a coherent package, which either was part of a larger debris transported within a matrix (i.e., larger than core scale) or a rafted block. The inferred relocated block at site GeoB 13804 is located about 3–4 km downslope of the prominent scarp, which constitutes the most probable source of the landslide (Figure 1). Large tabular blocks that were transported km wide during mass transport events similar to the inferred scenario at our study site occur for example off Angola [*Gee et al.*, 2005], off Norway [*Longva et al.*, 2003], and at the northern Svalbard margin [*Vanneste et al.*, 2006; *Winkelmann et al.*, 2008]. The low undrained shear strength measured within the relocated package (Figure 3) may suggest that its strength was reduced during transport on the rough surface predefined by older MTDs, but that the mass transport was sufficiently small and sufficiently low in energy to prevent a complete loss of the block's internal structure and geochemical pore water signature. An interpretation of the youngest event to be comparably small is further supported by Parasound data, which do not allow distinguishing deposits from this most recent event from older gravity flow deposits cored at site GeoB 13804 and GeoB 13807 (for data of GeoB 13807 see *Krastel et al.* [2011]).

[32] Since the ^{210}Pb method allows dating sediments as far back in time as ~150 years, a time span that would lead to a considerable smoothing of the pore water profiles, the ^{210}Pb profile should cover the time or rather the sediment accumulation after (and possibly before) the suspected sliding event. We consider the scattered $^{210}Pb_{unsupp}$ values in the thin interval of 2–4 cm to be a result of varying (increasing) sediment accumulation that led to a dilution of $^{210}Pb_{unsupp}$ rather than reflecting a sudden deposition of remobilized material (e.g., from a turbidity current). This assumption is supported by the absence of a distinct layer of coarse material indicating redeposition at this depth upon visual MUC core inspection. The $^{210}Pb_{unsupp}$ profile suggests continuous sedimentation of the uppermost 11.5 cm (below no $^{210}Pb_{unsupp}$ detected), albeit with a drastic change of SRs at about 1988. A laminar flow of this part of the sediment column would be reflected by a strong scatter of ^{210}Pb or (in the case that the eroded material was older than 150 years) overall low or absent $^{210}Pb_{unsupp}$ activities [e.g., *Garcia-Orellana et al.*, 2006; *Huh et al.*, 2006; *Alexander and Lee*, 2009] and can thus be excluded. We hypothesize that the observed drastic change of the SR at about 1988 indicates the timing of the youngest MTD event.

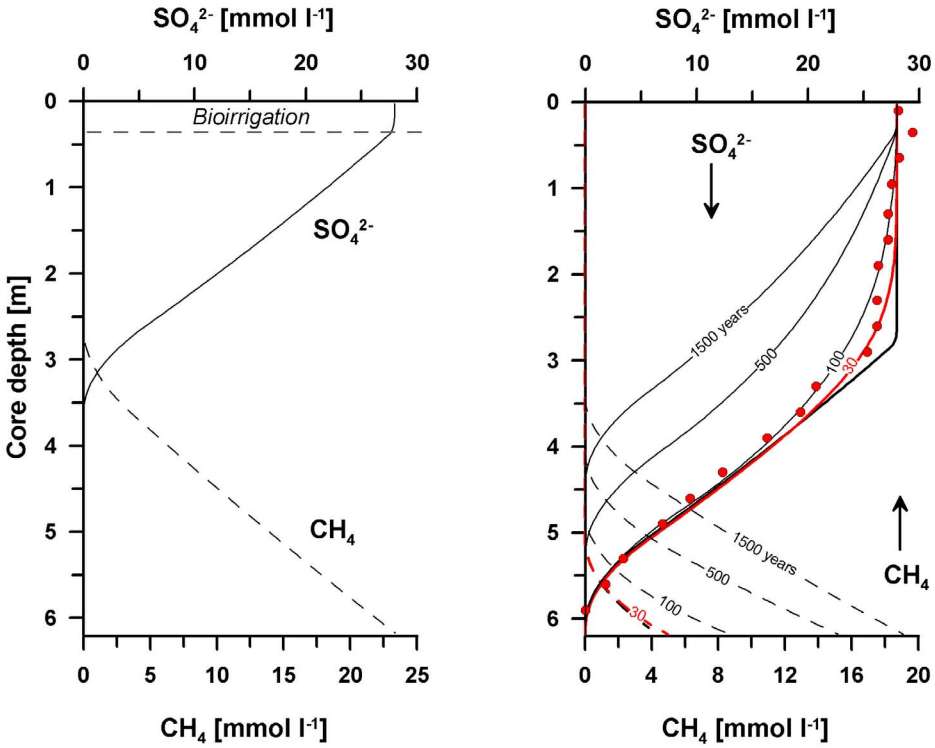

Figure 6. The graph on the left side shows the starting conditions of the geochemical transport and reaction model, i.e., the situation before deposition of the MTD. A constant CH_4 source at 8 m depth was applied. On the right side, the development of the SO_4^{2-} profile after the inferred deposition of the MTD at site GeoB 13804 is shown. The best fit of between model result and the measured data (red dots) is reached after about 30 years. However, after 30 years the profile is already reasonably smoothed. Thus, this estimate is regarded as a maximum age of the observed SO_4^{2-} profile.

The sediment below 4 cm might represent the top of a coherently relocated package from the nearby upper headwall. The sediment above 4 cm depth is interpreted as postevent sedimentation (Figure 5). The reasons for the change to extremely high SRs in the late 1980s remain speculative. The increase might be explained by postfailure slope readjustment of the headwall that supplies sediment to the area downslope or by changed current velocities in the study area favoring high sediment accumulation at the core location. It could also be related to increased sediment supply by the Río de la Plata plume.

5.2. Geochemical Modeling

[33] Regardless of its original source, the SO_4^{2-} profile will develop into a concave-up and finally a linear shape over time if the process that caused the kink shape profile is not active anymore. *Zabel and Schulz* [2001] and *Hensen et al.* [2003] used the diffusive re-equilibration of the SO_4^{2-} profile to date young MTDs. We set up a comparable simulation to estimate the maximum age of the kink-shaped SO_4^{2-} profile at the study site.

[34] For determining the CH_4 flux for the start of the simulation (steady state situation; Figure 5d), we considered only the part of the SO_4^{2-} profile below 2.43 m and "shifted" this section toward the sediment surface considering bioirrigation within in the uppermost 0.35 m (Figure 6). In other words, we subtracted or "removed" the youngest part of the sediment column (the suspected recent MTD and overlying recent sediment drape). The measured CH_4 could not be used for the simulation because conventional sampling techniques like those applied here always lead to considerable degassing amounting to up to 99.8% [e.g., *Dickens et al.*, 1997]. To determine the CH_4 flux into the SMTZ, we applied the approaches of *Borowski et al.* [1996] and *Niewöhner et al.* [1998], which are based on the reaction stoichiometry for the use of SO_4^{2-} and CH_4 during AOM. The CH_4 concentration determined for 8.0 m sediment depth (40 mM) produces an upward CH_4 flux that corresponds to the measured downward directed SO_4^{2-} flux. This CH_4 concentration is lower than the concentration in pore water equilibrated with gas hydrate (55 mM) as calculated after *Tishchenko et al.* [2005] for the in

situ pressure, salinity, and temperature. For AOM, a maximum reaction rate (R_{max} = 0.1 mol dm^{-3} yr^{-1}) was defined to produce a broad SMTZ with overlapping CH_4 and SO_4^{2-} profiles. That rate was used as long as the reactants were available in sufficient amounts (0th order kinetics). For lower concentrations of the reactants, the AOM rate was determined based on 2nd order kinetics. The reaction-specific change in concentration at a specific sediment depth ($\Delta C_{s,d}$) was calculated as follows:

$$\Delta C_{s,d} = R_{s,d} \times dt_{num} \times SC_{s,d} \quad (2)$$

where $R_{s,d}$ (in mol l^{-1} yr^{-1}) is the reaction rate, dt_{num} is the time step used in the model run, and $SC_{s,d}$ is a stoichiometric factor (for further details see *Hensen et al.* [2003] and *Riedinger et al.* [2005]). Diffusion coefficients were corrected for tortuosity [*Boudreau*, 1997] using the temperature of the water mass overlying the sediment (North Atlantic Deep Water: 3.5°C). The physical parameters of the water mass were measured during a CTD (conductivity/temperature/depth) sensor deployment at 36°10.28′S and 51°44.10′W during cruise M78/3 in June 2009. Bottom water concentrations of the chemical species derived from the MUC deployment define the upper boundary conditions. The lower boundary of the model is defined as an open boundary for all solutes except for CH_4, which means that the gradient of the last two cells is extrapolated to allow diffusion across the boundary. For the steady state situation (simulated to determine the CH_4 flux), a SR of 0.08 cm yr^{-1}, as deduced from the $^{210}Pb_{unsupp}$ data, was used. The mass movement event was simulated by shifting the steady state pore water profiles downward by the thickness of the MTD and assigning bottom water SO_4^{2-} concentrations of 28 mM to all cells above 2.4 m (Figure 6). Subsequently, the simulation was continued using the average postevent SR of 0.18 cm yr^{-1}. A compilation of all input parameters for the simulation runs is given in Table 2.

[35] The simulation of the SO_4^{2-} profile development shows that the best fit between modeled and measured SO_4^{2-} data at the study site is reached after 30 years (Figure 6). At this time, the profile shows, however, already a concave-up curvature. Therefore we consider 30 years to be the maximum age of the observed SO_4^{2-} profile. In fact, this result is irrespective of the actual cause for the nonsteady state SO_4^{2-} profile as long as the process that initiated the formation of the kink is inactive.

5.3. Earthquakes as Possible Trigger for the Slope Failure?

[36] Although our data do not allow for conclusively identifying the source of the supposed recent MTD, it is most probable that it is related to mass transport resulting from slope failure along the scarp to the northwest of site GeoB 13804 (Figure 1). Both, ^{210}Pb dating and the results of the geochemical modeling, hint to a possible landslide in the study area max. thirty years ago. The age range obtained from geochemical dating overlaps with one of the largest historically documented earthquakes that stroke this region on June 26, 1988. The earthquake with a magnitude 5.2 m_b nucleated in about 30 km depth, and its epicenter was located about 70 km to the southwest of site GeoB 13804 (Figure 1) [*Assumpção*, 1998; *Benavídez Sosa*, 1998]. Seismic ground shaking during this 1988 earthquake would thus be a plausible candidate to have triggered slope failures along the upper scarp and subsequent downslope mass transport.

[37] In order to test this hypothesis, we use probabilistic Limit Equilibrium slope stability calculations to back analyze critical seismic ground accelerations needed to initiate slope failures in the study area (see section 3.8). For simplistic reasons and due to the fact that extent, source, and geometry of the youngest (presumably 1988) landslide are not well constrained, we do not aim to explicitly model this specific event, but explore first-order general structures, seabed geomorphology, and available geotechnical property data (as summarized in section 4; see also Figures S2–S4) to generically investigate boundary conditions for earthquake-triggered slope failure scenarios representative of the study area. We then discuss obtained results with respect to the hypothesized 1988 event. We assume that the undisturbed slope above the prominent scarp represents a realistic prefailure slope and that submarine landslides were initiated by translational sliding along a 2 to 2.5° inclined failure plane in 75 (+/−25) m subsurface depth. This assumption is justified by acoustic subsurface images showing evenly stratified, 2 to 2.5° inclined reflections representing the general hemipelagic stratigraphic layering. The reflections are truncated by the upper scarp. A parallel reflection at the base of the scarp is continued at the base of the multistage MTD seaward of the scarp and is thus interpreted as the main failure plane (Figure 1 and also *Krastel et al.* [2011, Figure 4] showing a parallel profile to the NE of our studied transect). The subseafloor depth of this reflection in "undis-

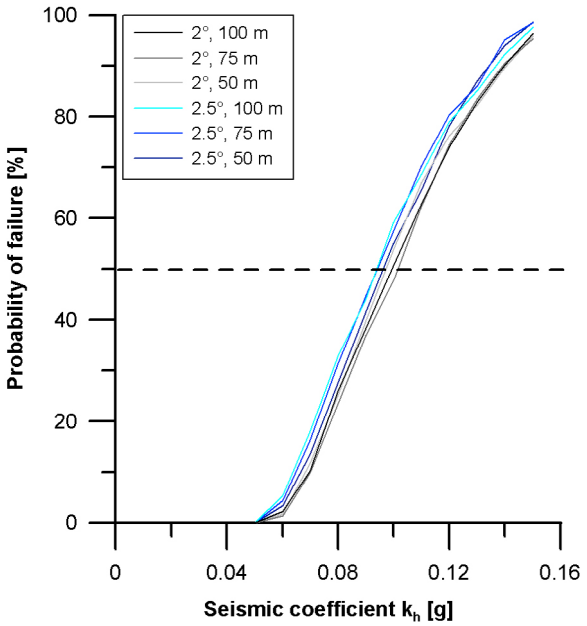

Figure 7. Probability of slope failure as a function of the simulated seismic coefficient k_h in the study area. The simulation was performed for a uniform slope with slope angles (α) of 2 and 2.5° and a subsurface depth of failure surface of 75 ± 25 m, as inferred from geophysical data (see text). The dashed line indicates a probability for slope failure of 50%.

turbed" slope segments above the headwall scarp (and thus the inferred failure plane depth) increases toward NE ~50 to ~100 m, as shown by Parasound and multibeam data. We therefore use this depth range as varying input parameter for our stability model. The overall translational geometry of the observed mass movement justifies the general assumption of the infinite slope model. Sediment cores from upslope of the headwall scarp (GeoB 13803-2, GeoB 13808-1, and GeoB 13854-1; see locations in Figure 1 and Table 1) generally show uniform hemipelagic mud, with constant bulk densities of 1.58 g cm^{-3} (+/−0.1 g cm^{-3}) and linearly increasing undrained shear strength values (1.5 kPa m^{-1}; +/−0.7 kPa m^{-1}) (see Figures S2–S4). This supports the assumption of a uniform slope model of homogenous fine-grained sediments for which an undrained failure criterion can be applied. Table 3 summarizes all input parameters and their variability as used for the probabilistic slope stability calculations.

[38] Results from slope stability calculations representing observed general submarine landslide features in the study area reveal stable slopes under static loading condition that may only fail if a lower minimum of additional seismic ground acceleration of 5.5% g (gravitational acceleration) is reached during earthquake shaking (Figure 7). The probability of failure increases with increasing ground accelerations and the slope should fail with a probability of >50% if the earthquake produces ground accelerations >9.75% g.

[39] In order to compare these results with ground motion intensities induced by the 1988 A.D. magnitude 5.2 earthquake, an empirical seismic attenuation relationship by *Campbell and Bozorgnia* [2008] was applied to estimate the median ground motions of peak ground acceleration at our study site. We use their equation 1 for magnitudes <5.5, nonspecified fault mechanism and a factor 2 for shallow site response of marine sediments with low shear velocities:

$$\ln(a) = (c_0 + c_1 M) + \left[(c_4 + c_5 M)\ln\left(\sqrt{R_{RUP}^2 + c_6^2}\right)\right] \quad (3)$$

where a is the horizontal peak ground acceleration as fraction of the gravitational acceleration (g), M is the earthquake magnitude, R_{RUP} is the epicentral distance and $c_{0–6}$ are empirical coefficients (c_0 = −1.715, c_1 = 0.500, c_4 = −2.118, c_5 = 0.170, c_6 = 5.60 [*Campbell and Bozorgnia*, 2008]). Accounting for uncertainties in epicentral location and magnitude [*Assumpção*, 1998, and references therein] in the order of 10 km and 0.1 magnitude units, respectively, solving equation (3) for a reveals estimates for horizontal ground motions at the study site during the 1988 earthquake ranging between 2% g and 4% g. These estimates are slightly lower than the minimum required seismic ground accelerations needed to trigger translational slope failure along 2 to 2.5° inclined slopes observed as general features in the study area, as reconstructed from our slope stability model.

[40] The general slope stability model may not fully represent the inferred scenario of retrogressive failure along the headwall scarp for the youngest (presumably 1988) landslide event. Slope angles of the headwall itself are steeper (up to 10°) and initial failure may in fact be rotational. Further possible preconditioning factors along the headwall scarp result from the older landslide, which caused a reduction in the mean stress and increase in shear stresses in the sediment present in the back wall [e.g., *Kvalstad et al.*, 2005]. Also, the general slope stability calculation does not include pore pressures and the preconditioning is set to normally consolidated and hydrostatic. This is mainly because there are no data available from cores or drilling in the study area for constraining possible in situ over-

pressures. A recent study by *Stigall and Dugan* [2010] in the Gulf of Mexico, however, has shown that overpressure can be caused by high sedimentation and lateral fluid flow, reducing slope stability significantly to such low levels that even a magnitude 5 earthquake at epicentral distance of up to 140 km was sufficient to eventually have initiated observed past failures at the study site. In our study area, overpressures are likely to be present, as indicated by the high sedimentation rates (see discussion of ^{210}Pb data in section 4.2) and the generally low-permeable nature of fine-grained hemipelagic sediments that may not drain the sediment sufficiently during fast compaction. All these above mentioned preconditioning factors, however, would rather reduce the stability compared to the scenario used for our first-order model assumption. We therefore interpret the critical seismic ground accelerations from our slope stability calculations as upper-limit maximal requirement to initiate failure. The observed most recent mass movement event, which likely reactivated a preexisting headwall scarp preconditioned at lower stability condition, could thus have been initiated at lower seismic ground shaking intensities.

[41] Taking this into account and given that the discrepancy of estimated ground motions and the calculated minimum acceleration needed to trigger failure is relatively small (i.e., 1.5% g), we conclude that the 1988 earthquake is a plausible trigger for the observed sedimentological and geochemical features associated with the youngest slide event observed at our study site, if likely additional weakening processes, such as headwall geometry and excess pore pressure, preconditioned the slope toward failure.

6. Conclusions

[42] At the continental slope off Uruguay, kink-shaped pore water profiles are associated with a sediment body which appears as an acoustically transparent unit with a hummocky surface in sediment echosounder data. Sedimentological, geotechnical, and geochemical solid phase data hint to a recent mass wasting event as possible reason for the nonsteady state condition of the pore water system at the study site GeoB 13804. The inferred subrecent MTD overlies an older gravity flow deposit that was not completely recovered during coring. Geochemical transport and reaction modeling indicates a maximum age of the most recent MTD of 30 years. The event could, thus, have been related to an m_b 5.2 earthquake that hit the area in 1988. Slope stability analysis reveals that earthquakes in this order of magnitude are potential triggers for instabilities in the study area, if additional weakening processes preconditioned the slope for failure.

[43] The complexity of integrating all results from the individual data sets shows that an approach using just one method is highly risky in order to interpret the structure and evolution of a MTD or MTC. A multidisciplinary approach seems to be essential to decipher relevant processes in a comprehensive view. Therefore, more interdisciplinary studies like this one are necessary to reach a holistic understanding of submarine mass movements.

Acknowledgments

[44] We gratefully acknowledge the support of Captain Baschek, the crew of R/V *Meteor*, and the scientists on board during cruise M78/3. Natascha Riedinger is greatly acknowledged for her support during the cruise, for providing TOC data, and for reviewing the manuscript in its early stage. Tim Ferdelmann and Andrea Schipper are thanked for their assistance with the ^{210}Pb samples. We thank Jana Friedrich for help with the interpretation of the ^{210}Pb data set and Kerstin Nöthen for support with CoTReM. Gert J. de Lange is acknowledged for fruitful discussions during the writing process. We are indebted to two anonymous reviewers for their constructive comments. This study was funded by the Deutsche Forschungsgemeinschaft (DFG) in the framework of the International Graduate College "Proxies in Earth History" (EUROPROX) and the Research Center/Cluster of Excellence "The Ocean in the Earth System" (MARUM). We acknowledge further financial support from the Helmholtz Association (AWI) and the Cluster of Excellence "The Future Ocean." All data are available from the database Pangaea (http://www.pangaea.de).

References

Adler, M., C. Hensen, F. Wenzhöfer, K. Pfeifer, and H. D. Schulz (2001), Modeling of calcite dissolution by oxic respiration in supralysoclinal deep-sea sediments, *Mar. Geol.*, *177*(1–2), 167–189, doi:10.1016/S0025-3227(01)00130-X.

Alexander, C. R., and H. J. Lee (2009), Sediment accumulation on the Southern California Bight continental margin during the twentieth century, in *Earth Science in the Urban Ocean: The Southern California Continental Borderland*, edited by H. J. Lee and W. R. Normark, *Spec. Pap. Geol. Soc. Am.*, *454*, 69–87, doi:10.1130/2009.2454(2.4).

Aller, R. C. (1983), The importance of the diffusive permeability of animal burrow linings in determining marine sediment chemistry, *J. Mar. Res.*, *41*(2), 299–322, doi:10.1357/002224083788520225.

Aller, R. C., N. E. Blair, Q. Xia, and P. D. Rude (1996), Remineralization rates, recycling, and storage of carbon in Amazon shelf sediments, *Cont. Shelf Res.*, *16*, 753–786, doi:10.1016/0278-4343(95)00046-1.

Appleby, P. G., and F. Oldfield (1978), The calculation of ^{210}Pb dates assuming a constant rate of supply of unsupported ^{210}Pb to the sediment, *Catena*, *5*, 1–8, doi:10.1016/S0341-8162(78)80002-2.

Assumpção, M. (1998), Seismicity and stresses in the Brazilian passive margin, *Bull. Seismol. Soc. Am.*, *88*(1), 160–169.

Barnes, R. O., and E. D. Goldberg (1976), Methane production and consumption in anoxic marine sediments, *Geology*, *4*(5), 297–300, doi:10.1130/0091-7613(1976)4<297:MPACIA>2.0.CO;2.

Benavídez Sosa, A. (1998), Sismicidad y sismotectónica en Uruguay, *Fis. Tierra*, *10*, 167–186.

Bianchi, A. A., A. R. Piola, and G. J. Collino (2002), Evidence of double diffusion in the Brazil-Malvinas Confluence, *Deep Sea Res., Part I*, *49*(1), 41–52, doi:10.1016/S0967-format0637(01)00039-5.

Bleil, U., et al. (1994), Report and preliminary results of Meteor Cruise M29/2, Montevideo–Rio de Janeiro, 15.07.1994–08.08.1994 report, 153 pp., Univ. of Bremen, Bremen, Germany.

Blum, P. (1997), Physical properties handbook: A guide to the shipboard measurement of physical properties of deep-sea cores, *Tech. Note 26*, Ocean Drill. Program, College Station, Tex.

Boetius, A., K. Ravenschlag, C. J. Schubert, D. Rickert, F. Widdel, A. Gieseke, R. Amann, B. B. Jørgensen, U. Witte, and O. Pfannkuche (2000), A marine microbial consortium apparently mediating anaerobic oxidation of methane, *Nature*, *407*, 623–626, doi:10.1038/35036572.

Borowski, W. S., C. K. Paull, and W. Ussler (1996), Marine pore-water sulfate profiles indicate in situ methane flux from underlying gas hydrate, *Geology*, *24*(7), 655–658, doi:10.1130/0091-7613(1996)024<0655:MPWSPI>2.3.CO;2.

Boudreau, B. P. (1997), *Diagenetic Models and Their Implementation: Modeling Transport and Reactions in Aquatic Sediments*, 414 pp., Springer, Berlin.

Boyce, R. E. (1977), Deep Sea Drilling Project procedures for shear strength measurement of clayey sediment using modified Wykeham Farrance laboratory vane apparatus, *Initial Rep. Deep Sea Drill. Proj.*, *36*, 1059–1068.

Brennecke, W. (1921), *Die Ozeanographischen Arbeiten der Deutschen Antarktischen Expedition 1911–1912*, 214 pp., Hammerich and Lesser, Hamburg, Germany.

Bryn, P., K. Berg, C. F. Forsberg, A. Solheim, and T. J. Kvalstad (2005), Explaining the Storegga Slide, *Mar. Pet. Geol.*, *22*(1–2), 11–19, doi:10.1016/j.marpetgeo.2004.12.003.

Campbell, K. W., and Y. Bozorgnia (2008), NGA ground motion model for the geometric mean horizontal component of PGA, PGV, PGD and 5% damped linear elastic response spectra for periods ranging from 0.01 to 10 s, *Earthquake Spectra*, *24*(1), 139–171, doi:10.1193/1.2857546.

Cline, J. D. (1969), Spectrophotometric determination of hydrogen sulfide in natural waters, *Limnol. Oceanogr.*, *14*(3), 454–458, doi:10.4319/lo.1969.14.3.0454.

Deacon, G. E. R. (1937), The hydrology of the Southern Ocean, 124 pp., Cambridge Univ. Press, London.

de Lange, G. J. (1983), Geochemical evidence of a massive slide in the southern Norwegian Sea, *Nature*, *305*, 420–422, doi:10.1038/305420a0.

Dickens, G. R., C. K. Paull, and P. J. Wallace (1997), Direct measurement of in situ methane quantities in a large gas-hydrate reservoir, *Nature*, *385*, 426–428, doi:10.1038/385426a0.

Fossing, H., T. G. Ferdelman, and P. Berg (2000), Sulfate reduction and methane oxidation in continental margin sediments influenced by irrigation (South–East Atlantic off Namibia), *Geochim. Cosmochim. Acta*, *64*(5), 897–910, doi:10.1016/S0016-7037(99)00349-X.

Franke, D., S. Neben, S. Ladage, B. Schreckenberger, and K. Hinz (2007), Margin segmentation and volcano-tectonic architecture along the volcanic margin off Argentina/Uruguay, South Atlantic, *Mar. Geol.*, *244*(1–4), 46–67.

Fredlund, D. G., and J. Krahn (1977), Comparison of slope stability methods of analysis, *Can. Geotech. J.*, *14*(3), 429–439, doi:10.1139/t77-045.

Garcia-Orellana, J., E. Gràcia, A. Vizcaino, P. Masqué, C. Olid, F. Martínez-Ruiz, E. Piñero, J. A. Sanchez-Cabeza, and J. Dañobeitia (2006), Identifying instrumental and historical earthquake records in the SW Iberian margin using ^{210}Pb turbidite chronology, *Geophys. Res. Lett.*, *33*, L24601, doi:10.1029/2006GL028417.

Gee, M. J. R., R. L. Gawthorpe, and J. S. Friedmann (2005), Giant striations at the base of a submarine landslide, *Mar. Geol.*, *214*, 287–294, doi:10.1016/j.margeo.2004.09.003.

Gordon, A. L., and C. L. Greengrove (1986), Geostrophic circulation of the Brazil-Falkland confluence, *Deep Sea Res., Part A*, *33*(5), 573–585, doi:10.1016/0198-0149(86)90054-3.

Grant, J. A., and R. Schreiber (1990), Modern swathe sounding and subbottom profiling technology for research applications: The Atlas Hydrosweep and Parasound Systems, *Mar. Geophys. Res.*, *12*(1–2), 9–19, doi:10.1007/BF00310559.

Grasshoff, K., K. Kremling, and M. Ehrhardt (1999), *Methods of Seawater Analysis*, 3rd ed., 600 pp., Wiley, Weinheim, Germany, doi:10.1002/9783527613984.

Guilderson, T. P., L. Burckle, S. Hemming, and W. R. Peltier (2000), Late Pleistocene sea level variations derived from the Argentine Shelf, *Geochem. Geophys. Geosyst.*, *1*(12), 1055, doi:10.1029/2000GC000098.

Haeckel, M., B. P. Boudreau, and K. Wallmann (2007), Bubble-induced porewater mixing: A 3-D model for deep porewater irrigation, *Geochim. Cosmochim. Acta*, *71*(21), 5135–5154, doi:10.1016/j.gca.2007.08.011.

Haese, R., C. Meile, P. Van Cappellen, and G. J. de Lange (2003), Carbon geochemistry of cold seeps: Methane fluxes and transformation in sediments from Kazan mud volcano, eastern Mediterranean Sea, *Earth Planet. Sci. Lett.*, *212*, 361–375, doi:10.1016/S0012-821X(03)00226-7.

Hampton, M. A., H. J. Lee, and J. Locat (1996), Submarine landslides, *Rev. Geophys.*, *34*(1), 33–59, doi:10.1029/95RG03287.

Hensen, C., M. Zabel, K. Pfeifer, T. Schwenk, S. Kasten, N. Riedinger, H. D. Schulz, and A. Boetius (2003), Control of sulfate pore-water profiles by sedimentary events and the significance of anaerobic oxidation of methane for the burial of sulfur in marine sediments, *Geochim. Cosmochim. Acta*, *67*(14), 2631–2647, doi:10.1016/S0016-7037(03)00199-6.

Hernández-Molina, F. J., M. Paterlini, R. Violante, P. Marshall, M. de Isasi, and L. Somoza (2009), Contourite depositional system on the Argentine Slope: An exceptional record of the influence of Antarctic water masses, *Geology*, *37*(6), 507–510, doi:10.1130/G25578A.1.

Hinz, K., S. Neben, B. Schreckenberger, H. A. Roeser, M. Block, K. G. d. Souza, and H. Meyer (1999), The Argentine continental margin north of 48°S: Sedimentary successions, volcanic activity during breakup, *Mar. Pet. Geol.*, *16*(1), 1–25, doi:10.1016/S0264-8172(98)00060-9.

Huh, C. A., C. C. Su, C. H. Wang, S. Y. Lee, and I. T. Lin (2006), Sedimentation in the Southern Okinawa Trough–

Rates, turbidites and a sediment budget, *Mar. Geol.*, *231*(1–4), 129–139, doi:10.1016/j.margeo.2006.05.009.

Kasten, S., M. Zabel, V. Heuer, and C. Hensen (2003), Processes and signals of nonsteady-state diagenesis in deep-sea sediments and their pore waters, in *The South Atlantic in the Late Quaternary: Reconstruction of Mass Budget and Current Systems*, edited by G. Wefer, S. Mulitza, and V. Ratmeyer, pp. 431–459, Springer, Berlin.

Klaus, A., and M. T. Ledbetter (1988), Deep-sea sedimentary processes in the Argentine Basin revealed by high-resolution seismic records (3.5 kHz echograms), *Deep Sea Res., Part A*, *35*(6), 899–917, doi:10.1016/0198-0149(88)90067-2.

Krastel, S., et al. (2011), Sediment dynamics and geohazards off Uruguay and the de la Plata River region (Northern-Argentina), *Geo Mar. Lett.*, *31*(4), 271–283, doi:10.1007/s00367-011-0232-4.

Kvalstad, T. J., L. Andresen, C. F. Forsberg, K. Berg, P. Bryn, and M. Wangen (2005), The Storegga slide: Evaluation of triggering sources and slide mechanics, *Mar. Pet. Geol.*, *22*, 245–256, doi:10.1016/j.marpetgeo.2004.10.019.

Ladd, C. C., and R. Foott (1974), New design procedure for stability of soft clays, *J. Geotech. Eng. Div. Am. Soc. Civ. Eng.*, *100*(GT7), 763–786.

Locat, J., and H. J. Lee (2002), Submarine landslides: Advances and challenges, *Can. Geotech. J.*, *39*, 193–212, doi:10.1139/t01-089.

Lonardi, A. G., and M. Ewing (1971), Sediment transport and distribution in the Argentine Basin. 4. Bathymetry of the continental margin. Argentine Basin and other related provinces. Canyons and sources of sediments, *Phys. Chem. Earth*, *8*, 79–121, doi:10.1016/0079-1946(71)90016-4.

Longva, O., N. Janbu, L. H. Blikra, and R. Bøe (2003), The 1996 Finneidfjord Slide; seafloor failure and slide dynamics, in *Submarine Mass Movements and Their Consequences*, edited by J. Locat and J. Mienert, pp. 531–538, Kluwer Acad., Dordrecht, Netherlands, doi:10.1007/978-94-010-0093-2_58.

Löwemark, L., and P. Schäfer (2003), Ethological implications from a detailed X-ray radiograph and C-14 study of the modern deep-sea Zoophycos, *Palaeogeogr. Palaeoclimatol. Palaeoecol.*, *192*(1–4), 101–121, doi:10.1016/S0031-0182(02)00681-8.

Mazumdar, A., A. L. Paropkari, D. V. Borole, B. R. Rao, N. H. Khadge, S. M. Karisiddaiah, M. Kocherla, and H. M. Joäo (2007), Pore-water sulphate concentration profiles of sediment cores from Krishna-Godavari and Goa basins, India, *Geochem. J.*, *41*, 259–269, doi:10.2343/geochemj.41.259.

Möller, O. O., Jr., A. R. Piola, A. C. Freitas, and E. J. D. Campos (2008), The effects of river discharge and seasonal winds on the shelf off southeastern South America, *Cont. Shelf Res.*, *28*(13), 1607–1624, doi:10.1016/j.csr.2008.03.012.

Morgenstern, N. R., and V. E. Price (1965), The analysis of the stability of general slip surfaces, *Geotechnique*, *15*(1), 79–93, doi:10.1680/geot.1965.15.1.79.

Mörz, T., E. A. Karlik, S. Kreiter, and A. Kopf (2007), An experimental setup for fluid venting in unconsolidated sediments: New insights to fluid mechanics and structures, *Sediment. Geol.*, *196*(1–4), 251–267, doi:10.1016/j.sedgeo.2006.07.006.

Niewöhner, C., C. Hensen, S. Kasten, M. Zabel, and H. D. Schulz (1998), Deep sulfate reduction completely mediated by anaerobic methane oxidation in sediments of the upwelling area off Namibia, *Geochim. Cosmochim. Acta*, *62*(3), 455–464, doi:10.1016/S0016-7037(98)00055-6.

Palma, E. D., R. P. Matano, and A. R. Piola (2008), A numerical study of the Southwestern Atlantic Shelf circulation: Stratified ocean response to local and offshore forcing, *J. Geophys. Res.*, *113*, C11010, doi:10.1029/2007JC004720.

Piola, A. R., and R. P. Matano (2001), Brazil and Falklands (Malvinas) currents, in *Encyclopedia of Ocean Sciences*, edited by J. H. Steele, K. K. Turekian, and S. A. Thorpe, pp. 340–349, Academic, San Diego, Calif., doi:10.1006/rwos.2001.0358.

Piola, A. R., R. P. Matano, E. D. Palma, O. O. Möller, and E. J. D. Campos (2005), The influence of the Plata River discharge on the western South Atlantic shelf, *Geophys. Res. Lett.*, *32*, L01603, doi:10.1029/2004GL021638.

Piola, A. R., S. I. Romero, and U. Zajaczkovski (2008), Space-time variability of the Plata plume inferred from ocean color, *Cont. Shelf Res.*, *28*, 1556–1567, doi:10.1016/j.csr.2007.02.013.

Reeburgh, W. S. (1976), Methane consumption in Cariaco Trench waters and sediments, *Earth Planet. Sci. Lett.*, *28*(3), 337–344, doi:10.1016/0012-821X(76)90195-3.

Riedinger, N., K. Pfeifer, S. Kasten, J. F. L. Garming, C. Vogt, and C. Hensen (2005), Diagenetic alteration of magnetic signals by anaerobic oxidation of methane related to a change in sedimentation rate, *Geochim. Cosmochim. Acta*, *69*(16), 4117–4126, doi:10.1016/j.gca.2005.02.004.

Robbins, J. A. (1978), Geochemical and geophysical applications of radioactive lead, in *Biogeochemistry of Lead in the Environment*, edited by J. O. Nriagu, pp. 285–393, Elsevier, Amsterdam.

Schnabel, M., D. Franke, M. Engels, K. Hinz, S. Neben, V. Damm, S. Grassmann, H. Pelliza, and P. R. Dos Santos (2008), The structure of the lower crust at the Argentine continental margin, South Atlantic at 44°S, *Tectonophysics*, *454*(1–4), 14–22, doi:10.1016/j.tecto.2008.01.019.

Schulz, H. D. (2006), Quantification of early diagenesis: Dissolved constituents in pore water and signals in the solid phase, in *Marine Geochemistry*, edited by H. D. Schulz and M. Zabel, pp. 73–124, Springer, Berlin, doi:10.1007/3-540-32144-6_3.

Seeberg-Elverfeldt, J., M. Schlüter, T. Feseker, and M. Kölling (2005), Rhizon sampling of porewaters near the sediment-water interface of aquatic systems, *Limnol. Oceanogr. Methods*, *3*, 361–371, doi:10.4319/lom.2005.3.361.

Stigall, J., and B. Dugan (2010), Overpressure and earthquake initiated slope failure in the Ursa region, northern Gulf of Mexico, *J. Geophys. Res.*, *115*, B04101, doi:10.1029/2009JB006848.

Strasser, M., S. Stegmann, F. Bussmann, F. S. Anselmetti, B. Rick, and A. Kopf (2007), Quantifying subaqueous slope stability during seismic shaking: Lake Lucerne as model for ocean margins, *Mar. Geol.*, *240*(1–4), 77–97, doi:10.1016/j.margeo.2007.02.016.

ten Brink, U. S., H. J. Lee, E. L. Geist, and D. Twichell (2009), Assessment of tsunami hazard to the US East Coast using relationships between submarine landslides and earthquakes, *Mar. Geol.*, *264*(1–2), 65–73, doi:10.1016/j.margeo.2008.05.011.

Tishchenko, P., C. Hensen, K. Wallmann, and C. S. Wong (2005), Calculation of the stability and solubility of methane hydrate in seawater, *Chem. Geol.*, *219*(1–4), 37–52, doi:10.1016/j.chemgeo.2005.02.008.

Tsumune, D., M. Aoyama, K. Hirose, F. O. Bryan, K. Lindsay, and G. Danabasoglu (2011), Transport of ^{137}Cs in the Southern Hemisphere in an ocean general circulation model, *Prog. Oceanogr.*, *89*, 38–48.

Uliana, M. B., K. T. Biddle, and J. Cerdan (1989), Mesozoic extension and formation of Argentine sedimentary basins, in *Extensional Tectonics and Stratigraphy of the North Atlantic Margins*, edited by A. J. Tankard and H. R. Balkwill, *AAPG Mem.*, *46*, 519–614.

Vanneste, M., J. Mienert, and S. Bünz (2006), The Hinlopen Slide: A giant, submarine slope failure on the northern Svalbard margin, Arctic Ocean, *Earth Planet. Sci. Lett.*, *245*, 373–388, doi:10.1016/j.epsl.2006.02.045.

Wenzhöfer, F., M. Adler, O. Kohls, C. Hensen, B. Strotmann, S. Boehme, and H. D. Schulz (2001), Calcite dissolution driven by benthic mineralization in the deep-sea: In situ measurements of Ca^{2+}, pH, pCO_2 and O_2, *Geochim. Cosmochim. Acta*, *65*(16), 2677–2690, doi:10.1016/S0016-7037(01)00620-2.

Winkelmann, D., W. Geissler, J. Schneider, and R. Stein (2008), Dynamics and timing of the Hinlopen/Yermak Megaslide north of Spitsbergen, Arctic Ocean, *Mar. Geol.*, *250*(1–2), 34–50, doi:10.1016/j.margeo.2007.11.013.

Zabel, M., and H. D. Schulz (2001), Importance of submarine landslides for non-steady state conditions in pore water systems—Lower Zaire (Congo) deep-sea fan, *Mar. Geol.*, *176*(1–4), 87–99, doi:10.1016/S0025-3227(01)00164-5.

Ziebis, W., S. Forster, M. Huettel, and B. B. Jørgensen (1996), Complex burrows of the mud shrimp *Callianassa truncata* and their geochemical impact in the sea bed, *Nature*, *382*, 619–622, doi:10.1038/382619a0.